Image reconstruction in spherical-wave intensity diffraction tomography

Mark A. Anastasio, Daxin Shi, and Yin Huang

Department of Biomedical Engineering, Illinois Institute of Technology, Chicago, Illinois 60616

Greg Gbur

Department of Physics and Optical Science, University of North Carolina–Charlotte, Charlotte, North Carolina 28223

Received December 15, 2004; revised manuscript received April 22, 2005; accepted May 6, 2005

A reconstruction theory for intensity diffraction tomography (I-DT) has been proposed that permits reconstruction of a weakly scattering object without explicit knowledge of phase information. We investigate the I-DT reconstruction problem assuming an incident (paraxial) spherical wave and scanning geometries that employ fixed source-to-object distances. Novel reconstruction methods are derived by identifying and exploiting tomographic symmetries and the rotational invariance of the problem. An underlying theme is that symmetries in tomographic imaging systems can facilitate solutions for phase-retrieval problems. A preliminary numerical investigation of the developed reconstruction methods is presented. © 2005 Optical Society of America

OCIS codes: 110.6960, 290.3200, 120.5050.

1. INTRODUCTION

Diffraction tomography[1–4] (DT) is a well-established imaging method used to determine the complex-valued refractive-index distribution of a weakly scattering object. The success of DT imaging in optical applications has been limited because it requires explicit knowledge of the phase of the measured wave fields, which can pose well-known experimental difficulties.[5] To circumvent the phase-retrieval problem, a theory of intensity DT (I-DT) has been proposed[6,7] that replaces explicit phase measurements on a single detector plane by intensity measurements on two or more different parallel planes at each tomographic view angle. Because I-DT addresses a fundamental inverse scattering problem, advancements in I-DT reconstruction theory will benefit a wide range of noninterferometric optical and coherent x-ray imaging modalities. In addition to improving the efficacy of existing imaging applications,[5,8–10] such advancements may prompt novel applications. The original I-DT reconstruction theory assumed plane-wave irradiation and directly related the intensity measurements at a given tomographic view angle to certain spatial-frequency components of the object function. Accordingly, the phase-retrieval problem is solved implicitly in I-DT during the process of reconstructing the object function. Unlike phase-retrieval methods based on the transport-of-intensity equation,[11,12] the transmitted wave fields are not required to be paraxial in I-DT.

We have recently generalized I-DT reconstruction theory to the case where the probing wave field is a spherical wave produced by a point source located a finite distance from the scatterer.[13] The spherical-wave I-DT reconstruction theory[13] employed assumptions regarding the placement of the point source and detector planes that coincided with those of a previous study of spherical-wave DT.[14] As in the plane-wave case, explicit phase measurements were replaced by measurements of the transmitted wave-field intensities on different parallel detector planes at each tomographic view angle.

A distinct feature of the spherical-wave I-DT reconstruction theory was that it required the point-source-to-object distance to be changed in a prescribed way before the intensity measurement on the second detector plane was acquired (at each tomographic view angle). This requires an extra degree of motion in the tomographic scanning that is undesirable because it can introduce errors into the measurement data and/or increase the time needed to perform the imaging scan. We demonstrated that, in principle, image reconstruction in spherical-wave I-DT could be accomplished assuming scanning geometries that had fixed source-to-object distances. However, explicit methods used to perform such image reconstructions were not identified.

In this paper we address the tomographic reconstruction problem for spherical-wave I-DT assuming scanning geometries that have fixed source-to-object distances. Although we are interested in studying optical wave fields that possess polarization, we will be considering only weak scattering problems in which a scalar description of the wave field is adequate (see Ref. 15, Section 13.1). The need to vary the source-to-object distance between intensity measurements is circumvented through the identification and exploitation of tomographic symmetries and the rotationally invariant nature of the problem. Two reconstruction methods are derived that are equivalent mathematically but utilize different sets of symmetries implicitly. The reconstruction methods are predicted to produce virtually identical images when applied to consistent measurement data, but distinct images when applied to inconsistent (e.g., noisy) measurement data. Prelimi-

nary numerical investigations of the developed methods are presented to demonstrate their use and corroborate our theoretical assertions.

2. BACKGROUND

Below we review the salient features of spherical-wave I-DT reconstruction theory as described in Ref. 13. To facilitate the description of the tomographic scanning geometry, we introduce a rotated Cartesian coordinate system $\mathbf{r}=(x,y_r,z_r)$, shown in Fig. 1, which is related to a reference system $\mathbf{r}=(x,y,z)$ by a rotation about the x axis such that $y_r=y\cos\phi+z\sin\phi$ and $z_r=z\cos\phi-y\sin\phi$. The angle ϕ is measured from the positive y axis. Throughout this paper, coordinates that have a subscript r will be associated with the rotated system. The unit vectors $\mathbf{s}_1$, $\mathbf{s}_{2,r}(\phi)$, and $\mathbf{s}_{0,r}(\phi)$ indicate the directions of the positive x, y_r, and z_r axes, respectively. Unless it is needed, the ϕ dependence of the unit vectors $\mathbf{s}_{2,r}(\phi),\mathbf{s}_{0,r}(\phi)$ will be suppressed.

A. Review of Spherical-Wave Intensity Diffraction Tomography

Consider the tomographic measurement geometry illustrated in Fig. 2. An incident spherical wave of the form

$$U_i(\mathbf{r})=\frac{\exp[jk|\mathbf{r}-\mathbf{r}_0|]}{|\mathbf{r}-\mathbf{r}_0|}, \tag{1}$$

with an assumed time dependence of $\exp[-j\omega t]$ ($j\equiv[-1]^{1/2}$), is employed to probe the scattering object. Here, $\mathbf{r}_0=(0,0,-z_0)$ denotes the location of the point source that is expressed in the (x,y_r,z_r) rotated coordinate system at orientation ϕ, and $k=2\pi/\lambda$ and λ denote the wavenumber and the wavelength of the probing field, respectively. The intensities of the forward-scattered wave fields are measured on the detector planes $z_r=d$ and

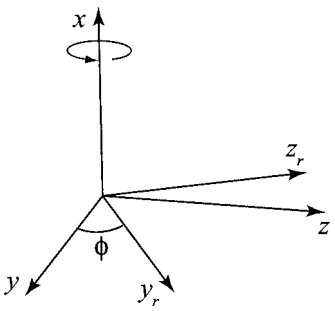

Fig. 1. Rotated coordinate system used to describe the tomographic measurement geometry.

$z_r=d+\Delta$. These intensity measurements will be denoted by the functions $I_{z_0}(x,y_r,\phi;d)$ and $I_{z_0}(x,y_r,\phi;d+\Delta)$, respectively, where the coordinates x and y_r describe locations on each detector plane. Note that a subscript has been added to these functions to make clear the dependence of the measured intensities on the source location z_0 (which can be different for the two measurements). By simultaneously rotating the point source and the measurement planes about the x axis (by varying the tomographic view angle ϕ), a set of intensity measurements is acquired that can be used to reconstruct an estimate of the object function $f(\mathbf{r})$. The object function is related to the complex-valued refractive-index distribution $n(\mathbf{r})$ as

$$f(\mathbf{r})=\frac{k^2}{4\pi}[n^2(\mathbf{r})-1]. \tag{2}$$

Beyond the scatterer, the total wave field can be expressed as

$$U(\mathbf{r})=U_i(\mathbf{r})\exp[\psi_{z_0}(\mathbf{r})], \tag{3}$$

where $\psi_{z_0}(\mathbf{r})$ is a complex phase function. Let $\psi_{z_0}(x,y_r,\phi;z_r)$ denote $\psi_{z_0}(\mathbf{r})$ evaluated on a plane of constant z_r and define

$$\hat{\psi}_{z_0}(u,v_r,\phi;z_r)=\frac{1}{(2\pi)^2}\int\int_{\mathbb{R}^2}dx\,dy_r\,\psi_{z_0}(x,y_r,\phi;z_r)\times\exp[-j(ux+v_ry_r)] \tag{4}$$

and

$$\hat{F}(\mathbf{K})=\frac{1}{(2\pi)^3}\int_{\mathbb{R}^3}d\mathbf{r}\,f(\mathbf{r})\exp[-j\mathbf{K}\cdot\mathbf{r}] \tag{5}$$

as the two-dimensional (2D) and three-dimensional (3D) Fourier transforms of $\psi_{z_0}(x,y_r,\phi;z_r)$ and $f(\mathbf{r})$, respectively. It proves convenient to define a modified complex phase function as

$$Q_{z_0}(x,y_r,\phi;z_r)=\frac{\psi_{z_0}(x,y_r,\phi;z_r)}{|\mathbf{r}_d-\mathbf{r}_0|}, \tag{6}$$

where $\mathbf{r}_d\equiv(x,y_r,z_r)$ denotes a point on the plane $z_r=d$. We assume that the object is weakly scattering and the first-order Rytov approximation[15] for the forward-scattering problem is valid. Additionally, we assume that both the source and the observation locations are sufficiently far from the scattering object so that the paraxial approximation may be used in the description of the incident wave field $U_i(\mathbf{r})$ and the Green's function that is associated with

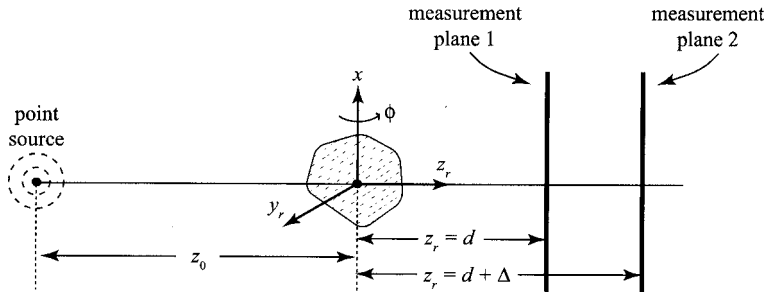

Fig. 2. Measurement geometry of spherical-wave I-DT.

the (linearized) forward-scattering problem. Under these conditions, the generalized Fourier diffraction projection theorem[14] indicates that

$$\hat{Q}_{z_0}(u,v_r,\phi;z_r)=\frac{(2\pi)^2 j}{z_0 w_\alpha \alpha^2}\underbrace{\hat{F}\left(\frac{u}{\alpha^2}\mathbf{s}_1+\frac{v_r}{\alpha^2}\mathbf{s}_{2,r}+(w_\alpha-k)\mathbf{s}_{0,r}\right)}_{\hat{F}[u/\alpha^2,v_r/\alpha^2,\phi]}\times\exp[j(w_\alpha-k)z_r], \tag{7}$$

where

$$\alpha\equiv\left[\frac{z_0}{z_r+z_0}\right]^{1/2} \tag{8}$$

is a scale parameter associated with the position of the source and detector plane,

$$w_\alpha\equiv\left[k^2-\left(\frac{u}{\alpha}\right)^2-\left(\frac{v_r}{\alpha}\right)^2\right]^{1/2}, \tag{9}$$

and $\hat{Q}_{z_0}(u,v_r,\phi;z_r)$ denotes the 2D Fourier transform of $Q_{z_0}(x,y_r,\phi;z_r)$. Throughout this paper, we will assume that w_α is a real-valued function of u and v_r, i.e., $(u/\alpha)^2+(v_r/\alpha)^2\leq k^2$. This reflects the fact that the contribution of evanescent wave modes to the measurement data is assumed to be negligible. Equation (7) demonstrates that the Fourier components of the modified phase function Q_{z_0} are directly related to the 3D Fourier components of the object function that reside on a shifted semiellipsoidal surface that intersects the origin and has an orientation ϕ. For convenience, we will employ the notation

$$\hat{F}[u/\alpha^2,v_r/\alpha^2,\phi]\equiv\hat{F}\left(\frac{u}{\alpha^2}\mathbf{s}_1+\frac{v_r}{\alpha^2}\mathbf{s}_{2,r}+(w_\alpha-k)\mathbf{s}_{0,r}\right) \tag{10}$$

to denote the Fourier components of the object that reside on this surface. Note that for the plane-wave case ($\alpha=1$), the surface reduces to the usual Ewald semisphere.[2] If the modified phase function Q_{z_0} is known at a collection of tomographic view angles ϕ, a certain band-limited region of 3D Fourier space can be specified. From this Fourier data, an estimate of $f(\mathbf{r})$ can be determined by use of a spherical-wave DT reconstruction algorithm.[16]

In spherical-wave I-DT, only the intensity $I_{z_0}(x,y_r,\phi;z_r)$ of the forward-scattered wave field is assumed to be measurable on a plane of constant z_r. Because the complex phase remains unknown, Eq. (7) cannot be employed directly for image reconstruction. An intensity data function can be defined as

$$D_{z_0}(x,y_r,\phi;z_r)=\frac{1}{|\mathbf{r}_d-\mathbf{r}_0|}\ln[I_{z_0}(x,y_r,\phi;z_r)], \tag{11}$$

whose 2D Fourier transform in the plane of constant z_r is denoted by $\hat{D}_{z_0}(u,v_r,\phi;z_r)$. We have shown[13] that

$$\hat{D}_{z_0}(u,v_r,\phi;z_r)=\frac{(2\pi)^2 j}{z_0 w_\alpha \alpha^2}\{\hat{F}[u/\alpha^2,v_r/\alpha^2,\phi]\exp[j(w_\alpha-k)z_r]-\hat{F}^*[-u/\alpha^2,-v_r/\alpha^2,\phi]\exp[-j(w_\alpha-k)z_r]\}, \tag{12}$$

where $*$ denotes the conjugate of a complex-valued quantity. Equation (12) relates the wave-field intensity on a plane of constant z_r to a linear combination of spatial-frequency components of the object function. This equation demonstrates clearly why, in general, frequency components of $f(\mathbf{r})$ cannot be reconstructed from a single intensity measurement.

B. Image Reconstruction: Geometries with Variable Source-to-Object Distances

For a fixed source-to-object distance z_0, let us consider that intensity measurements are acquired on the two planes $z_r=d$ and $z_r=d+\Delta(\Delta>0)$. Let

$$\alpha_1\equiv\left[\frac{z_0}{d+z_0}\right]^{1/2},\quad \alpha_2\equiv\left[\frac{z_0}{(d+\Delta)+z_0}\right]^{1/2}$$

describe the scale parameters associated with the two measurements [see Eq. (8)]. According to Eq. (12), $I_{z_0}(x,y_r,\phi;d)$ and $I_{z_0}(x,y_r,\phi;d+\Delta)$ are related to the object function as

$$\hat{D}_{z_0}(u,v_r,\phi;d)=\frac{(2\pi)^2 j}{z_0 w_{\alpha_1}\alpha_1^2}\{\hat{F}[u/\alpha_1^2,v_r/\alpha_1^2,\phi]\exp[j(w_{\alpha_1}-k)d]-\hat{F}^*[-u/\alpha_1^2,-v_r/\alpha_1^2,\phi]\exp[-j(w_{\alpha_1}-k)d]\}, \tag{13}$$

$$\hat{D}_{z_0}(u,v_r,\phi;d+\Delta)=\frac{(2\pi)^2 j}{z_0 w_{\alpha_2}\alpha_2^2}\{\hat{F}[u/\alpha_2^2,v_r/\alpha_2^2,\phi]\times\exp[j(w_{\alpha_2}-k)(d+\Delta)]-\hat{F}^*[-u/\alpha_2^2,-v_r/\alpha_2^2,\phi]\times\exp[-j(w_{\alpha_2}-k)(d+\Delta)]\}. \tag{14}$$

Equations (13) and (14) reveal that the measurements $I_{z_0}(x,y_r,\phi;d)$ and $I_{z_0}(x,y_r,\phi;d+\Delta)$ define a system of two equations with four unknowns, where the unknown quantities $\hat{F}[u/\alpha_1^2,v_r/\alpha_1^2,\phi]$, $\hat{F}^*[-u/\alpha_1^2,-v_r/\alpha_1^2,\phi]$, $\hat{F}[u/\alpha_2^2,v_r/\alpha_2^2,\phi]$, and $\hat{F}^*[-u/\alpha_2^2,-v_r/\alpha_2^2,\phi]$ represent distinct spatial-frequency components of the object that we wish to determine. These frequency components reside on semiellipsoidal Ewald surfaces as defined by Eq. (10). Note that this indeterminacy occurs because $\alpha_1\neq\alpha_2$.

To circumvent this problem, before acquiring the intensity measurement on the plane $z_r=d+\Delta$, we proposed[13] to change the source-to-object distance to the value $z_0'=z_0(d+\Delta)/d$. In this way, $\alpha_2=\alpha_1$, and $I_{z_0}(x,y_r,\phi;d)$ and $I_{z_0'}(x,y_r,\phi;d+\Delta)$ define a system of two equations with two unknowns whose solution yields

$$\hat{F}[u/\alpha_1^2, v_r/\alpha_1^2, \phi] = \frac{\hat{D}_{z_0}(u, v_r, \phi; d) - \hat{D}_{z_0'}(u, v_r, \phi; d+\Delta)\exp[j(w_{\alpha_1} - k)\Delta] z_0'/z_0}{j(2\pi)^2 \exp[j(w_{\alpha_1} - k)d](1 - \exp[j2(w_{\alpha_1} - k)\Delta])/(z_0 w_{\alpha_1} \alpha_1^2)}. \tag{15}$$

From this Fourier data, a spherical-wave DT reconstruction algorithm[14,16,17] can be employed to determine (an estimate of) the object function $f(\mathbf{r})$.

To use Eq. (15), the source-to-object distance must be changed from z_0 to z_0' before we acquire the intensity measurement on the plane $z_r = d + \Delta$. This introduces an extra degree of motion in the tomographic scanning procedure that is undesirable because it can introduce errors into the measurement data and/or increase the time needed to perform the imaging scan. We have demonstrated[13] that, in principle, image reconstruction in spherical-wave I-DT can be performed by use of a conventional in-line measurement geometry in which the source-to-object distance z_0 remains fixed. However, explicit reconstruction formulas used to achieve such reconstructions were not identified. This task is accomplished in the remainder of the paper.

3. FOURIER SPACE SYMMETRIES IN SPHERICAL-WAVE INTENSITY DIFFRACTION TOMOGRAPHY

Below we identify some explicit Fourier space symmetries that will facilitate the derivation of the reconstruction formulas in Section 4. These symmetries can be interpreted as tomographic symmetries in the sense that they relate values of the Fourier data $\hat{F}[\cdot, \cdot, \phi]$ that correspond to different tomographic view angles ϕ. As before, for a fixed z_0, let α_1 and α_2 denote the scale factors associated with the measurements on the planes $z_r = d$ and $z_r = d + \Delta$, respectively. Note that $\alpha_1 > \alpha_2$ because $\Delta > 0$. By definition [see Eq. (10)], we know that, for a fixed ϕ, the functions $\hat{F}[u/\alpha_1^2, v_r/\alpha_1^2, \phi]$ and $\hat{F}[u/\alpha_2^2, v_r/\alpha_2^2, \phi]$ describe Fourier components of the object function that reside on different semiellipsoidal surfaces. These surfaces coincide only at the origin of Fourier space ($u = v_r = 0$). However, by rotating one of the surfaces about the u axis (the direction $\mathbf{s}_1$), the two surfaces can be made to intersect at prescribed locations.

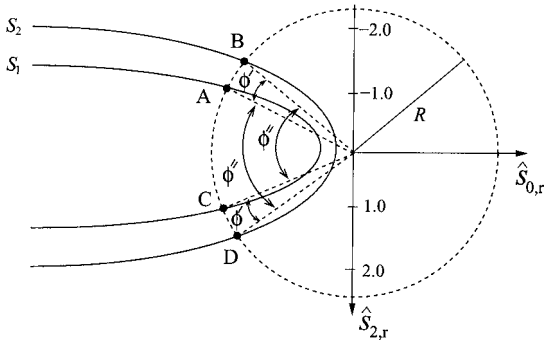

Fig. 3. Intersection of the ellipsoidal surfaces S_1 and S_2 with a plane of constant u in the 3D Fourier space ($u = 0.3$ in this example). The diagram was generated using $k = 1$, and S_1 and S_2 correspond to values $\alpha = 0.7$ and $\alpha = 0.5$, respectively.

To facilitate the discussions that follow, let S_1 and S_2 denote the 2D surfaces (of the semiellipsoids) that represent the domains of the functions $\hat{F}[u/\alpha_1^2, v_r/\alpha_1^2, \phi]$ and $\hat{F}[u/\alpha_2^2, v_r/\alpha_2^2, \phi]$, respectively, for a fixed ϕ. An example of the intersection of S_1 and S_2 with a particular plane of constant u is shown in Fig. 3. In the plane defined by $\mathbf{K} \cdot \mathbf{s}_1 = u/\alpha_1^2$, let A and C denote the two points of intersection of S_1 with a circle of radius R that is centered at the origin of this plane (see Fig. 3). In this plane, the points A and C correspond to locations $\nu_A = -(v_r/\alpha_1^2)\mathbf{s}_{2,r} + (w_{\alpha_1} - k)\mathbf{s}_{0,r}$ and $\nu_C = (v_r/\alpha_1^2)\mathbf{s}_{2,r} + (w_{\alpha_1} - k)\mathbf{s}_{0,r}$, respectively, and therefore

$$R \equiv \left[\left(\frac{v_r}{\alpha_1^2} \right)^2 + (w_{\alpha_1} - k)^2 \right]^{1/2}. \tag{16}$$

Similarly, let B and D denote the two points of intersection of S_2 with the same circle of radius R. The locations of points B and D in the plane $\mathbf{K} \cdot \mathbf{s}_1 = u/\alpha_1^2$ are given by $\nu_B = -(v_r'/\alpha_2^2)\mathbf{s}_{2,r} + (w'_{\alpha_2} - k)\mathbf{s}_{0,r}$ and $\nu_D = (v_r'/\alpha_2^2)\mathbf{s}_{2,r} + (w'_{\alpha_2} - k)\mathbf{s}_{0,r}$, respectively, where

$$w'_{\alpha_2} \equiv \left[k^2 - \left(\frac{u'}{\alpha_2} \right)^2 - \left(\frac{v_r'}{\alpha_2} \right)^2 \right]^{1/2}$$

and

$$u' = u \left(\frac{\alpha_2}{\alpha_1} \right)^2. \tag{17}$$

The frequencies v_r' must be real valued and satisfy the condition

$$R = \left[\left(\frac{v_r'}{\alpha_2^2} \right)^2 + (w'_{\alpha_2} - k)^2 \right]^{1/2}. \tag{18}$$

It can be seen from Fig. 3 that by rotating S_1 by an angle $-\phi'$ about the u axis, point A on S_1 can be made to coincide with point B on S_2. Similarly, if S_1 is rotated by an angle ϕ' about the u axis, point C on S_1 coincides with point D on S_2. It can be verified that these observations result from the symmetries

$$\hat{F}[u/\alpha_1^2, v_r/\alpha_1^2, \phi + \phi'] = \hat{F}[u'/\alpha_2^2, v_r'/\alpha_2^2, \phi], \tag{19}$$

where

$$v_r' = \mathrm{sgn}(v_r) \left[\frac{-b + [b^2 - 4ac]^{1/2}}{2a} \right]^{1/2}, \tag{20}$$

with $\mathrm{sgn}(v_r) \equiv 1$ for $v_r \geq 0$ and -1 otherwise, and

$$a = \left(\frac{1}{\alpha_2^4} - \frac{1}{\alpha_2^2}\right)^2, \tag{21a}$$

$$b = \frac{4k^2}{\alpha_2^4} - 2\left(R^2 + \left(\frac{u'}{\alpha_2}\right)^2\right)\left(\frac{1}{\alpha_2^4} - \frac{1}{\alpha_2^2}\right), \tag{21b}$$

$$c = \left(\frac{u'}{\alpha_2}\right)^4 + 2R^2\left(\frac{u'}{\alpha_2}\right)^2 + R^4 - 4k^2R^2 \tag{21c}$$

(see Appendix A for details). The angle ϕ' is given by

$$\phi' = -\arctan\left(\frac{v_r'/\alpha_2^2}{w'_{\alpha_2,r} - k}\right) + \arctan\left(\frac{v_r/\alpha_1^2}{w_{\alpha_1} - k}\right). \tag{22}$$

When $(u/\alpha_1)^2 + (v_r/\alpha_1)^2 \leq k^2$, v_r' and ϕ' are real-valued functions of u, v_r, α_1, and α_2.

Equation (19) relates the Fourier components on S_1 and S_2 that reside on the same halves of the Ewald surfaces [i.e., v_r and v_r' have the same sign in Eq. (19)]. However, by rotating S_1 by an angle ϕ'' about the u axis, as defined in Fig. 3, point C on S_1 can be made to correspond to point B on S_2. Similarly, by rotating S_1 by an angle $-\phi''$, point A on S_1 can be made to correspond to point D on S_2. It can be verified that these observations result from the symmetries

$$\hat{F}[u/\alpha_1^2, v_r/\alpha_1^2, \phi - \phi''] = \hat{F}[u'/\alpha_2^2, -v_r'/\alpha_2^2, \phi], \tag{23}$$

where

$$\phi'' = -\arctan\left(\frac{v_r'/\alpha_2^2}{w'_{\alpha_2} - k}\right) - \arctan\left(\frac{v_r/\alpha_1^2}{w_{\alpha_1} - k}\right). \tag{24}$$

From these observations, it can be seen that one can find information about a particular Fourier component of the object function in numerous distinct intensity measurements. No single intensity measurement or pair of measurements can determine this Fourier component; however, it can be determined by combining many intensity measurements in a nontrivial way. We consider two strategies for doing this in the next section.

4. RECONSTRUCTION METHODS

Here we derive and investigate two novel reconstruction methods for spherical-wave I-DT assuming scanning geometries with fixed source-to-object distances z_0. To accomplish this, we exploit the Fourier space symmetries described in Section 3 and an invariance property of the Fourier integral (specifically, the Fourier-shift theorem). For convenience, we will define

$$\hat{D}(u, v_r, \phi; z_r) \equiv \frac{\hat{D}_{z_0}(u, v_r, \phi; z_r) z_0 w_\alpha \alpha^2}{(2\pi)^2 j} \exp[-j(w_\alpha - k)z_r]. \tag{25}$$

In terms of this data function, according to Eq. (12), the intensity measurements acquired on the planes $z_r = d$ and $z_r = d + \Delta$ are related to the object function as

$$\hat{D}(u, v_r, \phi; d) = \hat{F}[u/\alpha_1^2, v_r/\alpha_1^2, \phi] - \hat{F}^*[-u/\alpha_1^2, -v_r/\alpha_1^2, \phi] \times \exp[-2j(w_{\alpha_1} - k)d], \tag{26}$$

where $(u/\alpha_1)^2 + (v_r/\alpha_1)^2 \leq k^2$ and

$$\hat{D}(u, v_r, \phi; d + \Delta) = \hat{F}[u/\alpha_2^2, v_r/\alpha_2^2, \phi] - \hat{F}^*[-u/\alpha_2^2, -v_r/\alpha_2^2, \phi] \times \exp[-2j(w_{\alpha_2} - k)(d + \Delta)], \tag{27}$$

where $(u/\alpha_2)^2 + (v_r/\alpha_2)^2 \leq k^2$.

A. Reconstruction Method 1

In this subsection we employ the set of symmetries described by Eq. (19) to derive a method for reconstruction of $f(\mathbf{r})$. A second reconstruction method that exploits the symmetries given by Eq. (23) is developed in Subsection 4.B.

Consider Eq. (27) evaluated at the frequencies $u = u'$ and $v_r = v_r'$:

$$\hat{D}(u', v_r', \phi; d + \Delta) = \hat{F}[u'/\alpha_2^2, v_r'/\alpha_2^2, \phi] - \hat{F}^*[-u'/\alpha_2^2, -v_r'/\alpha_2^2, \phi] \times \exp[-2j(w'_{\alpha_2} - k)(d + \Delta)], \tag{28}$$

where we recall that w'_{α_2} denotes w_{α_2} evaluated at the frequencies $u = u'$ and $v_r = v_r'$. By making use of the symmetry property in Eq. (19), Eq. (28) can be expressed as

$$\hat{D}(u', v_r', \phi; d + \Delta) = \hat{F}[u/\alpha_1^2, v_r/\alpha_1^2, \phi + \phi'(v_r)] - \hat{F}^*[-u/\alpha_1^2, -v_r/\alpha_1^2, \phi - \phi'(v_r)] \times \exp[-2j(w'_{\alpha_2} - k)(d + \Delta)], \tag{29}$$

where the dependence of ϕ' on v_r has been made explicit (although its dependence on u, α_1, and α_2 remain suppressed), and the property $\phi'(-v_r) = -\phi'(v_r)$ has been utilized. Because of the presence of the ϕ' terms in Eq. (29), Eqs. (29) and (26) still represent a 2×4 system that cannot be solved uniquely.

Because $\hat{D}(u, v_r, \phi; z_r)$ is a periodic function of ϕ, it can be expressed as the Fourier series

$$\hat{D}(u, v_r, \phi; z_r) = \sum_{n=-\infty}^{\infty} \hat{D}_n(u, v_r; z_r) \exp[jn\phi],$$

where

$$\hat{D}_n(u,u_r;z_r) = \frac{1}{2\pi}\int_0^{2\pi} d\phi \hat{D}(u,v_r,\phi;z_r)\exp[-jn\phi]. \quad (30)$$

On substituting from Eq. (26) into Eq. (30), one obtains

$$\hat{D}_n(u,v_r;d) = \hat{F}_n[u/\alpha_1^2,v_r/\alpha_1^2] - (\hat{F}_{-n}[-u/\alpha_1^2,-v_r/\alpha_1^2])^* \times \exp[-2j(w_{\alpha_1}-k)d], \quad (31)$$

where

$$\hat{F}_n[u/\alpha_1^2,v_r/\alpha_1^2] = \frac{1}{2\pi}\int_0^{2\pi} d\phi \hat{F}[u/\alpha_1^2,v_r/\alpha_1^2,\phi]\exp[-jn\phi]. \quad (32)$$

Similarly, on substituting from Eq. (29) into Eq. (30), one obtains

$$\hat{D}_n(u',v_r';d+\Delta) = \exp[jn\phi'(v_r)]\hat{F}_n[u/\alpha_1^2,v_r/\alpha_1^2] - \exp[-jn\phi'(v_r)](\hat{F}_{-n}[-u/\alpha_1^2,-v_r/\alpha_1^2])^* \times \exp[-2j(w'_{\alpha_{2,r}}-k)(d+\Delta)]. \quad (33)$$

We now find that Eqs. (31) and (33) represent a linearly independent system of two equations with two unknowns that can be solved to determine

$$\hat{F}_n[u/\alpha_1^2,v_r/\alpha_1^2] = \frac{\hat{D}_n(u,v_r;d) - \hat{D}_n(u',v_r';d+\Delta)\exp[jn\phi'(v_r) + 2j(w'_{\alpha_{2,r}}-k)(d+\Delta) - 2j(w_{\alpha_1}-k)d]}{1-\exp[2j(n\phi'(v_r) + (w'_{\alpha_{2,r}}-k)(d+\Delta) - (w_{\alpha_1}-k)d)]} \quad (34)$$

for $(u/\alpha_1)^2+(v_r/\alpha_1)^2 \leq k^2$. Equation (34) represents the sought-after reconstruction formula. From knowledge of $\hat{F}_n[u/\alpha_1^2,v_r/\alpha_1^2]$, or equivalently

$$\hat{F}[u/\alpha_1^2,v_r/\alpha_1^2,\phi] = \sum_{n=-\infty}^{\infty} \hat{F}_n[u/\alpha_1^2,v_r/\alpha_1^2]\exp[jn\phi], \quad (35)$$

an estimate of $f(\mathbf{r})$ can be reconstructed by use of a spherical-wave DT reconstruction algorithm.[16,17]

B. Reconstruction Method 2

In this subsection we employ the set of symmetries described by Eq. (23) to derive a second reconstruction method.

Consider Eq. (27) evaluated at the frequencies $u=u'$ and $v_r=-v_r'$:

$$\hat{D}(u',-v_r',\phi;d+\Delta) = \hat{F}[u'/\alpha_2^2,-v_r'/\alpha_2^2,\phi] - \hat{F}^*[-u'/\alpha_2^2,v_r'/\alpha_2^2,\phi] \times \exp[-j(w'_{\alpha_{2,r}}-k)(d+\Delta)]. \quad (36)$$

By making use of the symmetry property in Eq. (23), Eq. (36) can be expressed as

$$\hat{D}(u',-v_r',\phi;d+\Delta) = \hat{F}[u/\alpha_1^2,v_r/\alpha_1^2,\phi-\phi''(v_r)] - \hat{F}^*[-u/\alpha_1^2,-v_r/\alpha_1^2,\phi+\phi''(v_r)] \times \exp[-2j(w'_{\alpha_{2,r}}-k)(d+\Delta)], \quad (37)$$

where the dependence of ϕ'' on v_r has been made explicit (although its dependence on u, α_1, and α_2 remain suppressed), and the property $\phi''(-v_r)=-\phi''(v_r)$ has been utilized.

On substituting from Eq. (37) into Eq. (30), one obtains

$$\hat{D}_n(u',-v_r';d+\Delta) = \exp[-jn\phi''(v_r)]\hat{F}_n[u/\alpha_1^2,v_r/\alpha_1^2] - \exp[+jn\phi''(v_r)](\hat{F}_{-n}[-u/\alpha_1^2,-v_r/\alpha_1^2])^* \times \exp[-2j(w'_{\alpha_{2,r}}-k)(d+\Delta)]. \quad (38)$$

We find now that Eqs. (31) and (38) represent a linearly independent system of two equations with two unknowns that can be solved to determine

$$\hat{F}_n[u/\alpha_1^2,v_r/\alpha_1^2] = \frac{\hat{D}_n(u,v_r;d) - \hat{D}_n(u',-v_r';d+\Delta)\exp[-jn\phi''(v_r) + 2j(w'_{\alpha_{2,r}}-k)(d+\Delta) - 2j(w_{\alpha_1}-k)d]}{1-\exp[2j(-n\phi''(v_r) + (w'_{\alpha_{2,r}}-k)(d+\Delta) - (w_{\alpha_1}-k)d)]} \quad (39)$$

for $(u/\alpha_1)^2+(v_r/\alpha_1)^2 \leq k^2$. From knowledge of $\hat{F}_n[u/\alpha_1^2,v_r/\alpha_1^2]$, an estimate of $f(\mathbf{r})$ can be reconstructed by use of a DT reconstruction algorithm.

C. Comments on the Reconstruction Formulas

As discussed in Subsection 2.B, for a scanning geometry in which the source-to-object distance z_0 is fixed, the two intensity measurements acquired on the $z_r=d$ and $z_r=d+\Delta$ at a given tomographic view angle do not determine uniquely any of the Fourier components of the object function. To circumvent this difficulty, the reconstruction formulas derived in Subsections 4.A and 4.B make use of symmetries that relate Fourier components of the object function that reside on the two Ewald surfaces (corresponding to scale parameters α_1 and α_2) at different to-

mographic view angles. An important feature of the angular shifts denoted by ϕ' and ϕ'' in Eqs. (19) and (23), respectively, is that they do not depend on the tomographic view angle ϕ. This reflects that the I-DT imaging model is rotationally invariant. Because of their invariance to angular shifts, reconstruction formulas for determination of the Fourier series expansion coefficients $\hat{F}_n[u/\alpha_1^2, v_r/\alpha_1^2]$ were determined readily. The proposed reconstruction methods for spherical-wave I-DT are fundamentally distinct from other I-DT reconstruction methods in the sense that they employ measurements from all tomographic view angles $\phi \in [0, 2\pi)$ for reconstruction of any specified Fourier component of the object function.

The inversion formulas given in Eqs. (34) and (39) are equivalent mathematically. In the absence of data inconsistencies and finite sampling effects, they will yield identical estimates of $\hat{F}_n[u/\alpha_1^2, v_r/\alpha_1^2]$. However, when the data contain inconsistencies, Eqs. (34) and (39) will generally produce distinct estimates of $\hat{F}_n[u/\alpha_1^2, v_r/\alpha_1^2]$. This is because Eqs. (34) and (39) exploit different Fourier space symmetries and therefore utilize different components of the measurement data to form the estimates of $\hat{F}_n[u/\alpha_1^2, v_r/\alpha_1^2]$. Numerical examples of this are provided in Section 5.

Equations (34) and (39) contain poles whose locations depend on d, Δ, k, and the measurement geometry (more specifically, α_1 and α_2). Because the collection of poles represents a set of measure zero, this presents no mathematical difficulties. In theory, the spherical-wave I-DT reconstruction methods specify exactly the same object function as the conventional spherical-wave DT method in Ref. 14. However, the poles can pose considerable practical difficulties when the methods are applied to discretely sampled and inconsistent measurement data. First, the poles are not uniformly spaced, and are generally difficult to avoid when we attempt to determine $\hat{F}_n[u/\alpha_1^2, v_r/\alpha_1^2]$ at uniformly spaced values of u and v_r. Simply setting $\hat{F}_n[u/\alpha_1^2, v_r/\alpha_1^2]=0$ at the location of the poles can lead to inaccuracies in the reconstructed image. Second, even if the poles are avoided, data errors can be greatly amplified when the denominators of Eqs. (34) and (39) take on small values, which occurs in the vicinity of poles. These observations indicate that the reconstruction methods will need to be regularized in practical applications. We refer the reader to Ref. 18 for an introduction to regularization methods applied to imaging problems. Alternatively, these problems can be circumvented if a third measurement plane is employed. Because the locations of the poles depend on d and Δ, the poles and their immediate neighborhoods can be avoided by use of an appropriate pair of detector planes. A simple demonstration of this implementation strategy is demonstrated in the next section. As in the plane-wave I-DT theory,[6,7] the zero-frequency component of the object function remains undetermined.

5. NUMERICAL RESULTS

We conducted a preliminary numerical investigation of the two spherical-wave I-DT reconstruction methods developed in Section 4.

A. Phantom and Simulation Data

The 2D mathematical phantom shown in Fig. 4 was utilized in our simulation studies. The length of the long axis of the largest ellipse (i.e., the background ellipse) was 0.92 mm, and the refractive-index values of the object are indicated in Fig. 4. The 2D scanning geometry is described in Fig. 5. The point source ($\lambda = 1 \times 10^{-5}$ m) was located at $z_r = -z_0 = -0.04$ m and three detector planes were positioned behind the object at $z_r = 0.04$, 0.044, and 0.05 m (i.e., $d = 0.04$ m, $\Delta_1 = 0.004$ m, and $\Delta_3 = 0.01$ m in Fig. 4). The three detector planes correspond to scale parameters $\alpha_1 = 0.707$, $\alpha_2 = 0.690$, and $\alpha_3 = 0.667$, respectively, via Eq. (8). Each detector array had a length of 5.12 cm and contained 2048 elements (therefore the detector sampling interval was $\Delta y_r = 25$ μm).

Because the phantom was comprised of uniform ellipses, its 2D Fourier transform was known analytically. The intensity data $I_{z0}(y_r, \phi; z_r)$ on the three detector arrays were calculated by use of Eqs. (11) and (12), with the u and x dependencies of the equations omitted. Intensity data were calculated at 360 evenly spaced tomographic view angles over the interval $[0, 2\pi)$. Note that the phantom was, by construction, a weakly scattering object. The deleterious effects of strong scattering[19,20] are not investigated in this work. To investigate the noise propagation properties of the reconstruction methods, the intensity data were treated as realizations of an uncorrelated Gaussian stochastic process that was characterized by its mean μ and standard deviation σ. When generating the noisy data, μ was set equal to the noiseless value of $I(y_r, \phi; z_r)$ at a given detector location and σ was chosen to satisfy $\sigma/\mu = 1.0\%$.

B. Reconstruction Procedure

Let $\hat{D}(v_r, \phi; d)$, $\hat{D}(v_r, \phi; d+\Delta_1)$, and $\hat{D}(v_r, \phi; d+\Delta_3)$ denote the Fourier data functions, as defined in Eq. (25), that correspond to the three detector planes. (Here and elsewhere, the u dependence of the equations will be omitted for this 2D example.) When computing these data functions, the one-dimensional fast-Fourier-transform (FFT) algorithm was employed to compute $\hat{D}_{z0}(v_r, \phi; z_r)$ [Eq. (12)] at uniformly spaced values of v_r from knowledge of $D_{z0}(y_r, \phi; z_r)$ [or equivalently, $I(y_r, \phi; z_r)$ via Eq. (11)] at uniformly spaced values of y_r. From the set of uniformly spaced values of v_r, the set of nonuniformly spaced values v_r' was computed by use of Eq. (20). Let $\hat{D}(v_r', \phi; d+\Delta_1)$ and $\hat{D}(v_r', \phi; d+\Delta_3)$ denote the Fourier data functions evaluated at the nonuniformly spaced frequencies v_r'. These data function values were determined by first increasing the sampling density of the uniformly spaced data $\hat{D}(v_r, \phi; d+\Delta_1)$ and $\hat{D}(v_r, \phi; d+\Delta_3)$ by a factor of 8 (by zero padding in the spatial domain), followed by a linear interpolation operation. In a similar way, the data function values $\hat{D}(-v_r', \phi; d+\Delta_1)$ and $\hat{D}(-v_r', \phi; d+\Delta_3)$ were determined. The Fourier series expansion coefficients $\hat{D}_n(v_r; d)$, $\hat{D}_n(v_r; d+\Delta_1)$, $\hat{D}_n(v_r; d+\Delta_3)$ $\hat{D}_n(-v_r'; d+\Delta_1)$, and $\hat{D}_n(-v_r'; d+\Delta_3)$ were calculated by applying the FFT algorithm to the sampled angular coordinate (ϕ) of the corresponding data functions.

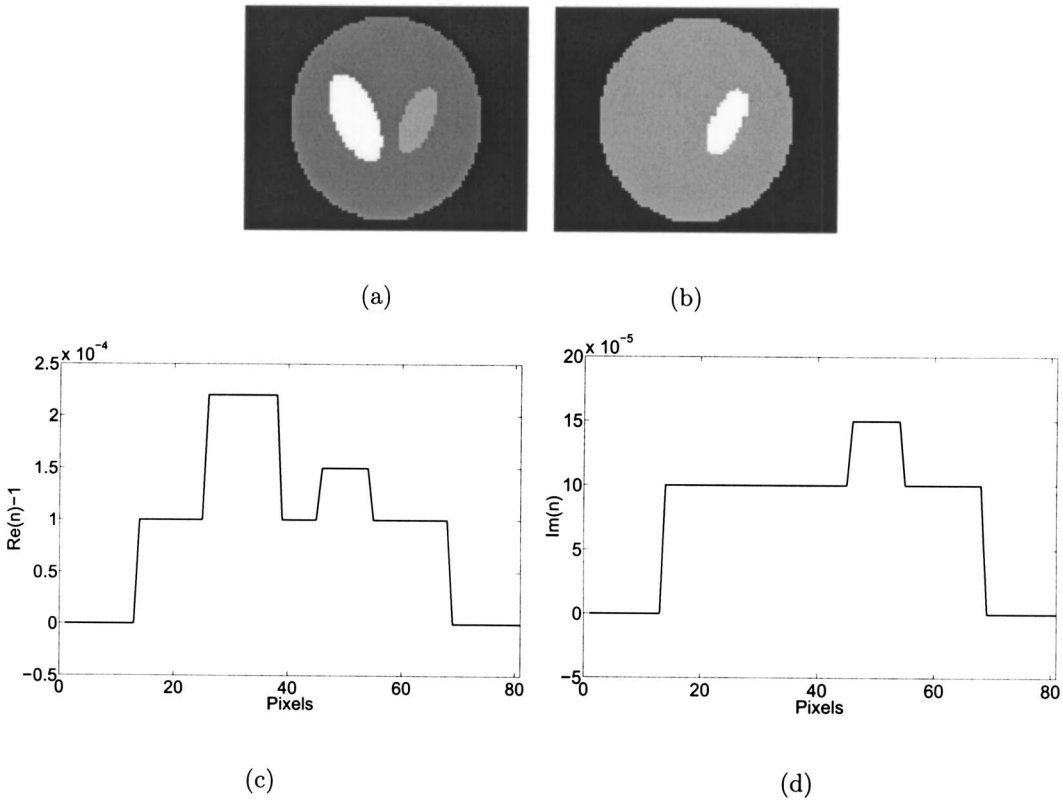

Fig. 4. (a) Real component of the phantom object. (b) Imaginary component of the phantom object. (c) Profile through the central row in (a). (d) Profile through the central row in (b).

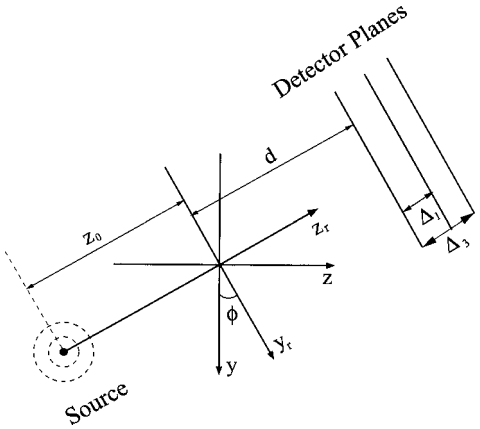

Fig. 5. Shown is the 2D scanning geometry employed in the numerical simulations. Intensity data were acquired on three detector planes at each view angle.

To demonstrate the feasibility of the proposed reconstruction methods, a simple strategy for utilization of the intensity data measured on the three detector planes was adopted. Let

$$F_n^{(i)}[v_r/\alpha_1^2] \equiv \frac{N_n^{(i)}[v_r]}{D_n^{(i)}[v_r]}, \tag{40}$$

where $N_n^{(i)}[v_r]$ and $D_n^{(i)}[v_r]$ represent the numerator and denominator, respectively, of Eq. (34) or Eq. (39) for the cases where $\Delta=\Delta_i$, $i=1,3$. Therefore $F_n^{(1)}[v_r/\alpha_1^2]$ is obtained by use of intensity data on detector planes one and two, and $F_n^{(3)}[v_r/\alpha_1^2]$ is obtained by use of intensity data on detector planes one and three. Although an estimate of $F_n[v_r/\alpha_1^2]$ could also be obtained by use of intensity data on the second and third detector planes, we do not make use of this fact here.

As discussed previously, the motivation for employing a three-detector-plane geometry is to avoid the problems associated with the singularities in the reconstruction formulas. In our reconstruction procedure, we implemented the following simple rule to achieve this:

$$F_n[v_r/\alpha_1^2] = \begin{cases} F_n^{(1)}[v_r/\alpha_1^2] & : \ |D_n^{(1)}[v_r]| \geqslant |D_n^{(3)}[v_r]| \\ F_n^{(3)}[v_r/\alpha_1^2] & : \ \text{otherwise.} \end{cases} . \tag{41}$$

In this way, for a given frequency component v_r, $F_n[v_r/\alpha_1^2]$ is determined by use of the detector plane pair that avoids encountering a singularity and minimizes the amplification of data inconsistencies. From the estimated $F_n[v_r/\alpha_1^2]$, an estimate of the object function $f(\mathbf{r})$ was obtained by use of the DT reconstruction algorithm in Ref. 21. The matrix size of the reconstructed images was 2048×2048 pixels, but only an 81×81 pixels subregion that contains the object is shown. Using these procedures, images were reconstructed from the noiseless and noisy simulated data sets by use of reconstruction methods 1 and 2.

C. Reconstructed Images

Noiseless reconstructions of the scattering object are shown in Fig. 6. The real and imaginary components of the refractive-index distribution $n(\mathbf{r})$ reconstructed from noiseless data by use of method 1 are shown in Figs. 6(a) and 6(b), respectively. The corresponding images reconstructed by use of method 2 are shown in Figs. 6(c) and 6(d). Profiles through the central rows of Figs. 6(a) and 6(c) are represented by the solid and dashed curves, respectively, in Fig. 7(a). Profiles through the central rows of Figs. 6(b) and 6(d) are represented by the solid and dashed curves, respectively, in Fig. 7(b). Because the profiles are nearly identical, the dashed curves are obscured in these figures. These results reveal that, in the absence of data noise, reconstruction methods 1 and 2 produce images that are nearly identical and represent low-pass-filtered estimates of the true refractive-index distribution. This is consistent with our claim that the methods are identical mathematically.

Noisy reconstructions of the scattering object are shown in Fig. 8. The real and imaginary components of the refractive-index distribution $n(\mathbf{r})$ reconstructed from noisy data by use of method 1 are shown in Figs. 8(a) and 8(b), respectively. The corresponding images reconstructed by use of method 2 are shown in Figs. 8(c) and 8(d). Profiles through the central rows of Figs. 8(a) and 8(c) are represented by the solid and dashed curves, respectively, in Fig. 9(a). Profiles through the central rows of Figs. 8(b) and 8(d) are represented by the solid and dashed curves, respectively, in Fig. 9(b). These results reveal that, in the presence of data noise, reconstruction methods 1 and 2 have a visually different response to that noise. This is so because the methods exploit different Fourier space symmetries and therefore utilize distinct

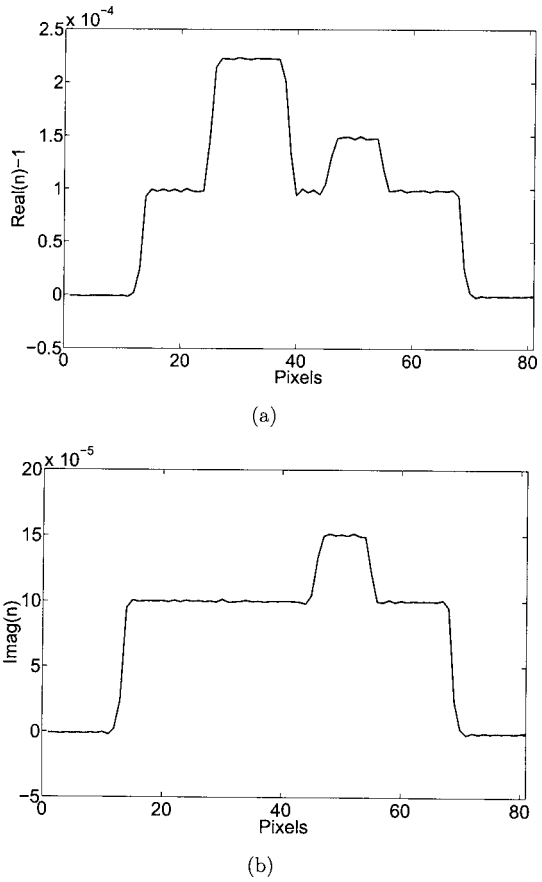

Fig. 7. (a) Profiles through the central rows of Figs. 6(a) and 6(c) are represented by the solid and dashed curves, respectively. (b) Profiles through the central rows of Figs. 6(b) and 6(d) are represented by the solid and dashed curves, respectively. In both graphs, the dashed curves are completely obscured by the solid curves.

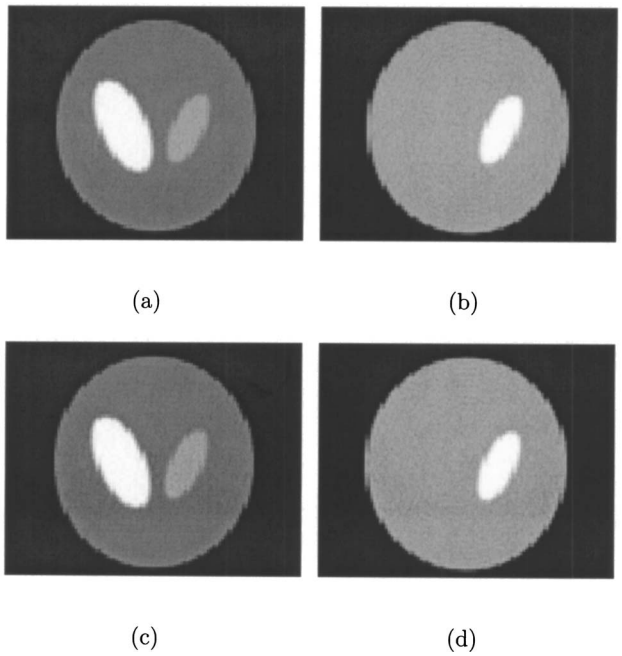

Fig. 6. (a) Real and (b) imaginary components of the refractive-index distribution $n(\mathbf{r})$ reconstructed from noiseless data by use of method 1. (c) and (d) The corresponding images reconstructed by use of method 2.

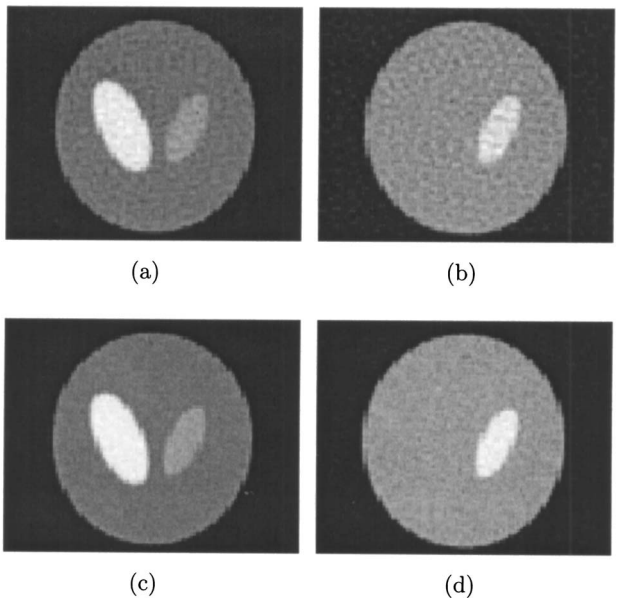

Fig. 8. (a) Real and (b) imaginary components of the refractive-index distribution $n(\mathbf{r})$ reconstructed from noisy data by use of method 1. (c) and (d) The corresponding images reconstructed by use of method 2.

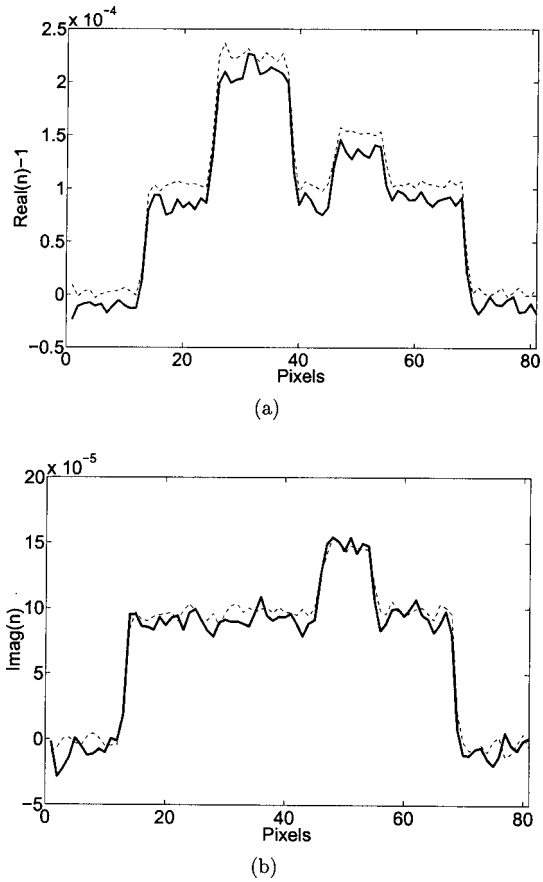

Fig. 9. (a) Profiles through the central rows of Figs. 8(a) and 8(c) are represented by the solid and dashed curves, respectively. (b) Profiles through the central rows of Figs. 8(b) and 8(d) are represented by the solid and dashed curves, respectively.

components of the measurement data to form the reconstructed images.

6. SUMMARY

Because it permits measurements of the wave-field phase to be replaced by measurements of the wave-field intensities, spherical-wave I-DT may be useful for tomographic optical imaging of semitransparent objects. A distinct feature of the previously proposed[13] spherical-wave I-DT reconstruction method was that it required the source-to-object distance of the scanning geometry to be changed in a prescribed way to acquire the intensity data at each tomographic view angle. This requires an extra degree of motion in the tomographic scanning that is undesirable because it can introduce errors into the measurement data and/or increase the time needed to perform the imaging scan. Although we demonstrated theoretically that spherical-wave I-DT could be implemented with scanning geometries that had fixed source-to-object distances, explicit methods for reconstructing images were not identified.

In this paper we developed tomographic reconstruction methods for spherical-wave I-DT assuming scanning geometries that have fixed source-to-object distances. The need to vary the source-to-object distance between intensity measurements was circumvented by the identification and exploitation of tomographic symmetries and the rotational invariance of the problem. Two reconstruction methods were derived that are equivalent mathematically but utilize different sets of symmetries implicitly. Preliminary numerical investigations of the developed methods were presented to demonstrate their use and corroborate our theoretical assertions.

An interesting and unique characteristic of the developed reconstruction methods is the manner in which they utilize the available intensity measurements. In most of the existing in-line holographic, or phase-retrieval-based, tomography techniques,[5,7,22–24] the intensity measurements acquired at a given tomographic view angle are processed independently of the intensity measurements acquired at all other view angles. For example, in phase-contrast tomography, two intensity measurements at a given tomographic view angle are utilized to determine the phase of the transmitted wave field at that view angle.[22–24] In plane-wave I-DT, a Fourier space relationship exists that relates two intensity measurements at a given tomographic view angle to certain spatial-frequency components of the object function. The developed reconstruction formulas for spherical-wave I-DT are expressed in terms of the Fourier series expansion coefficients of the object and data functions. Accordingly, the reconstruction of the Fourier components of the object function requires knowledge of the intensity measurements at *all* view angles, and therefore the processing of the intensity measurements at each view angle is not decoupled. To our knowledge, this is the first work to exploit tomographic symmetries for establishing a solution to a phase-retrieval problem.

Several features of the developed reconstruction methods remain topics for future investigations. In our simulation studies, a 2D object and three detector planes were assumed. It will be important to implement and investigate the methods for the full 3D problem. Additionally, suitable regularization strategies should be developed that can be employed when intensity data on only two detector planes are available at each tomographic view angle. Finally, the incorporation and investigation of multiple-scattering effects in I-DT is an interesting and important topic for future research.

APPENDIX A

Here we provide a derivation of the frequency variables u' and v_r' that first appear in Eqs. (19) and (23). Consider points A and B that correspond to the intersection of the surfaces S_1 and S_2 with a plane of constant u, as described in Section 3 and shown in Fig. 3. The locations of these points are given by $\mathbf{K}_A=(u/\alpha_1^2)\mathbf{s}_1-(v_r/\alpha_1^2)\mathbf{s}_{2,r}+(w_{\alpha_1}-k)\mathbf{s}_{0,r}$ and $\mathbf{K}_B=(u'/\alpha_2^2)\mathbf{s}_1-(v_r'/\alpha_2^2)\mathbf{s}_{2,r}+(w_{\alpha_2}-k)\mathbf{s}_{0,r}$, respectively. On substitution from Eq. (17), $\mathbf{K}_B$ can be expressed as $\mathbf{K}_B=(u/\alpha_1^2)\mathbf{s}_1-(v_r'/\alpha_2^2)\mathbf{s}_{2,r}+(w_{\alpha_2}-k)\mathbf{s}_{0,r}$. Therefore Eq. (17) dictates that points A and B reside on the same plane of constant u.

For the points A and B to reside on the same circle of radius R in this plane, v_r' must be an appropriate function of v_r, u, α_1, and α_2. To determine this function, we can employ the observation that v_r' must satisfy

$$R^2 = \left(\frac{v_r'}{\alpha_2^2}\right)^2 + (w'_{\alpha_2} - k)^2$$
$$= \left(\frac{v_r'}{\alpha_2^2}\right) + \left(\left[k^2 - \left(\frac{u'}{\alpha^2}\right) - \left(\frac{v_r'}{\alpha_2}\right)^2\right]^{1/2} - k\right)^2, \quad \text{(A1)}$$

where R is defined by Eq. (16). From Eq. (A1) one finds that v_r' satisfies the fourth-order equation

$$a(v_r')^4 + b(v_r')^2 + c = 0, \quad \text{(A2)}$$

where a, b, and c are defined in Eq. (21). The four roots of Eq. (A2) are

$$v_r'^{(1)} = -v_r'^{(2)} = \left[\frac{-b + [b^2 - 4ac]^{1/2}}{2a}\right]^{1/2}, \quad \text{(A3)}$$

$$v_r'^{(3)} = -v_r'^{(4)} = \left[\frac{-b - [b^2 - 4ac]^{1/2}}{2a}\right]^{1/2}. \quad \text{(A4)}$$

It can be verified that for $(u/\alpha_1)^2 + (v_r/\alpha_1)^2 \leq k^2$, $v_r'^{(1)}$ and $v_r'^{(2)}$ are real valued, while $v_r'^{(3)}$ and $v_r'^{(4)}$ are complex valued. Therefore $v_r'^{(3)}$ and $v_r'^{(4)}$ are not meaningful physically. The fact that there exist two (real-valued) values of v_r' that satisfy Eq. (A1) [or Eq. (A2)] reflects that S_2 intersects the circle of radius R at two locations, corresponding to a positive and negative value of v_r'. For example, in Fig. 3, $v_r'^{(1)}$ and $v_r'^{(2)}$ correspond to the points D and B, respectively.

ACKNOWLEDGMENTS

M. A. Anastasio thanks Xiaochuan Pan for the many interesting discussions of imaging symmetries that inspired this work. This work was supported in part by a grant from the Illinois Institute of Technology Research Institute (grant 5-54510-IITRI).

The corresponding author is Mark A. Anastasio (anastasio@iit.edu).

REFERENCES

1. E. Wolf, "Three-dimensional structure determination of semi-transparent objects from holographic data," Opt. Commun. **1**, 153–156 (1969).
2. E. Wolf, "Principles and development of diffraction tomography," in *Trends in Optics*, A. Consortini, ed. (Academic, 1996).
3. A. J. Devaney, "Diffraction tomography," in *Inverse Methods in Electromagnetic Imaging, Part 2*, W. M. Boerner, ed., NATO ASI Series (Reidel, 1983), pp. 1107–1135.
4. A. J. Devaney, "Geophysical diffraction tomography," IEEE Trans. Geosci. Remote Sens. **22**, 3–13 (1984).
5. T. Wedberg and J. Stamnes, "Quantitative imaging by optical diffraction tomography," Opt. Rev. **2**, 28–31 (1995).
6. G. Gbur and E. Wolf, "Diffraction tomography without phase information," Opt. Lett. **27**, 1890–1892 (2002).
7. G. Gbur and E. Wolf, "Hybrid diffraction tomography without phase information," J. Opt. Soc. Am. A **19**, 2194–2202 (2002).
8. V. Lauer, "New approach to optical diffraction tomography yielding a vector equation of diffraction tomography and a novel tomographic microscope," J. Microsc. (Oxford) **205**, 165–176 (2001).
9. T. C. Wedberg and J. J. Stamnes, "Recent results in optical diffraction microtomography," Meas. Sci. Technol. **7**, 414–418 (1996).
10. A. S. T. Beetz and C. Jacobsen, "Soft x-ray diffraction tomography: simulations and first experimental results," J. Phys. IV **104**, 31–34 (2003).
11. K. A. Nugent, T. E. Gureyev, D. Cookson, D. Paganin, and Z. Barnea, "Quantitative phase imaging using hard x-rays," Phys. Rev. Lett. **77**, 2961–2964 (1996).
12. M. R. Teague, "Deterministic phase retrieval: a Green's function solution," J. Opt. Soc. Am. **73**, 1434–1441 (1983).
13. G. Gbur, M. A. Anastasio, Y. Huang, and D. Shi, "Spherical-wave intensity diffraction tomography," J. Opt. Soc. Am. A **22**, 230–238 (2005).
14. A. J. Devaney, "Generalized projection-slice theorem for fan-beam diffraction tomography," Ultrason. Imaging **7**, 264–275 (1985).
15. M. Born and E. Wolf, *Principles of Optics* (Cambridge U. Press, 1999).
16. M. A. Anastasio and X. Pan, "An improved reconstruction algorithm for 3D diffraction tomography using spherical-wave sources," IEEE Trans. Biomed. Eng. **50**, 517–521 (2003).
17. Z. Lu, "Multidimensional structure diffraction tomography for varying object orientation through generalised scattered waves," Inverse Probl. **1**, 339–356 (1985).
18. M. Bertero and P. Boccacci, *Introduction to Inverse Problems in Imaging* (Institute of Physics, 1998).
19. M. Slaney, A. C. Kak, and L. Larsen, "Limitations of imaging with first-order diffraction tomography," IEEE Trans. Microwave Theory Tech. **32**, 860–874 (1984).
20. B. Chen and J. Stamnes, "Validity of diffraction tomography based on the first-Born and first-Rytov approximations," Appl. Opt. **37**, 2996–3006 (1998).
21. M. A. Anastasio and X. Pan, "Full- and minimal-scan reconstruction algorithms for fan-beam diffraction tomography," Appl. Opt. **40**, 3334–3345 (2001).
22. S. Mayo, T. Davis, T. Gureyev, P. Miller, D. Paganin, A. Pogany, A. Stevenson, and S. Wilkins, "X-ray phase-contrast microscopy and microtomography," Opt. Express **11**, 2289–2302 (2003).
23. A. Barty, K. A. Nugent, A. Roberts, and D. Paganin, "Quantitative phase tomography," Opt. Commun. **175**, 329–336 (2000).
24. T. Gureyev, T. Davis, A. Pogany, S. Mayo, and S. Wilkins, "Optical phase retrieval by use of first Born- and Rytov-type approximations," Appl. Opt. **43**, 2418–2430 (2004).